NANO LETTERS

Letter

pubs.acs.org/NanoLett

Single-Spin Dirac Fermion and Chern Insulator Based on Simple Oxides

Tianyi Cai,[†] Xiao Li,[‡,§,#] Fa Wang,[‡,§] Sheng Ju,[*,†] Ji Feng,[*,‡,§] and Chang-De Gong[∥,⊥]

[†]Department of Physics and Jiangsu Key Laboratory of Thin Films, Soochow University, Suzhou 215006, P. R. China

[‡]International Center for Quantum Materials, School of Physics, Peking University, Beijing 100871, P. R. China

[§]Collaborative Innovation Center of Quantum Matter, Beijing, P. R. China

[∥]Center for Statistical and Theoretical Condensed Matter Physics and Department of Physics, Zhejiang Normal University, Jinhua 321004, P. R. China

[⊥]National Laboratory of Solid State Microstructure and Department of Physics, Nanjing University, Nanjing 210093, P. R. China

Supporting Information

ABSTRACT: It is highly desirable to combine recent advances in the topological quantum phases with technologically relevant materials. Chromium dioxide (CrO_2) is a half-metallic material, widely used in high-end data storage applications. Using first-principles calculations, we show that a novel class of half semimetallic Dirac electronic phase emerges at the interface CrO_2 with TiO_2 in both thin film and superlattice configurations, with four spin-polarized Dirac points in momentum-space (***k***-space) band structure. When the spin and orbital degrees of freedom are allowed to couple, the CrO_2/TiO_2 superlattice becomes a Chern insulator without external fields or additional doping. With topological gaps equivalent to 43 K and a Chern number ±2, the ensuing quantization of Hall conductance to $\pm 2e^2/h$ will enable potential development of these highly industrialized oxides for applications in topologically high fidelity data storage and energy-efficient electronic and spintronic devices.

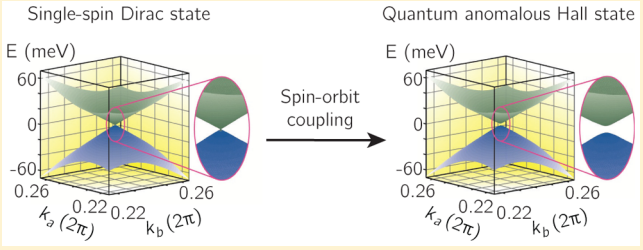

KEYWORDS: *Single-spin Dirac state, Chern insulator, CrO_2/TiO_2 heterostructure, first-principles calculations*

The defining feature of massless Dirac Fermions[1,2] is a linear energy dispersion, implying that a quasiparticle moves at a constant speed independent of its energy, as governed by relativistic quantum mechanics. The exploration of novel Dirac materials with *bulk* Dirac or Dirac−Weyl states remains a great challenge in condensed matter and materials physics.[3−10] It is very interesting to develop materials with single-spin Dirac points, which may be called a *half semimetal*. Half metals are a class of ferromagnetic materials in which the conduction is dominated by one spin component, while the other spin is gapped, which stands to enable reduced device size and nonvolatile memory. At a rudimentary level, a half semimetal will harbor the fascinating Dirac physics[1−10] all with a single spin. As a not-so-trivial consequence, it may lead to Chern insulators[11−14] or valleytronics materials[15−18] when the low-energy excitations turn massive. A Chern insulator exhibits quantum anomalous Hall (QAH) effect with a quantized, dissipationless transport from the chiral edge channels, in the absence of external magnetic field and the magnetic field-induced Landau levels. It was established experimentally recently in magnetically doped topological insulator at 30 mK.[14] Yet, there is no basic reason that this fundamental phenomenon can only be realized based on topological insulators. A half semimetal will be a viable precursor for the QAH phase, without the need for magnetic doping. For these reasons, it is highly desirable to achieve ferromagnetic half-semimetallic phase, which will significantly broaden the scope of the study of topological materials.

Precisely controlled growth of heterojunctions of oxides[19,20] offers a unique avenue for exploring novel topological phases, enjoying rich interplay of orbital, charge, spin, and lattice degrees of freedom.[21,22] In the letter, we investigate the possibility to fashion two-dimensional (2D) chromium dioxide (CrO_2) layers into single-spin Dirac states by interfacial orbital design, given that bulk CrO_2 is a robust half metal even at elevated temperatures[23−25] and widely used in enterprise-grade data storage. Based on first-principles calculations, we show that in heterostructures of CrO_2 and TiO_2, the d-orbitals of Cr are isolated into Dirac states, with four single-spin Dirac points in the 2D ***k***-space. Spin−orbit coupling (SOC) renders these Dirac nodes field-tunable; that is, they can continuously vary from massless to massive by aligning their magnetization. The non-Abelian Berry curvature is directly calculated using ab initio method, which indicates that the gapped CrO_2/TiO_2

Received: May 6, 2015
Revised: August 18, 2015
Published: August 25, 2015

DOI: 10.1021/acs.nanolett.5b01791
Nano Lett. 2015, 15, 6434−6439

superlattice with out-of-plane magnetization is a topological Chern insulator with a Chern number = ±2, having twice the chiral edge states available from the Chern insulator based on topological insulators.[12−14] We also propose a low-energy effective model Hamiltonian and discuss the role of symmetry for Dirac states in 2D CrO_2 systems. Experimental advances suggested by these theoretical proposals will pave the way toward field-tunable single-spin Dirac Fermions and high-temperature QAH states, with potential applications in spintronics as well as low-power and noise-tolerant quantum electronics.

Single-Spin Dirac Points. Both CrO_2 and TiO_2 have stable rutile (XO_2, X = Ti, Cr) phases. In the rutile structure, each metal atom, Cr or Ti, lies in the center of an octahedral cage formed by six oxygen atoms. These XO_6 octahedra share corners to form a three-dimensional network in the space group $P4_2/mnm$ (Figure 1a). We define local coordinates for the

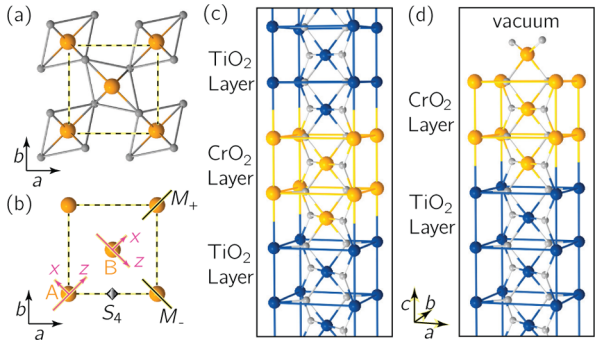

Figure 1. Structure and symmetry of rutile oxides and the heterostructures of CrO_2 and TiO_2. (a) Rutile structure cleaved along (001) plane, showing the XO_6 octahedra with two distinctive orientations. (b) Symmetry and local coordinates of a XO_2 unit cell. Here, we use *xyz* for the local coordinates and *abc* for the global orientation. (c) Structural model of the superlattice of CrO_2 and TiO_2. (d) Structural model of CrO_2 thin film on TiO_2 substrate. Orange, blue, and gray balls correspond to Cr, Ti, and O, respectively.

metal sites to account for two orientations of the oxygen octahedra, as depicted in Figure 1b. The X−O bonds along the crystallographic **a** ± **b** (or [110] and [1$\bar{1}$0]) directions are elongated. Consequently, the local symmetry of the distorted octahedral shell is D_{2h}, for which the principal 2-fold axis (i.e., the local *z* axis) can be aligned along the corresponding elongated X−O bonds. Crystallographic (1$\bar{1}$0) and (110) planes are planes of mirror symmetry of the distorted octahedra, which we call M_+ and M_-, respectively. The system also has a 4-fold rotoinversion, S_4. $M_\pm$ and S_4 constitute the generators of the lattice point group.

As shown in Figure 1c,d, we construct two types of CrO_2/TiO_2 heterostructures, i.e., superlattices of CrO_2 and TiO_2 and ultrathin films of CrO_2 coupled to a TiO_2 substrate, which both include the 2D CrO_2 layers, given that CrO_2/TiO_2 heterostructures are readily achievable.[24,25] While the superlattices inherit the S_4 and $M_\pm$ symmetries of the rutile structure, $M_\pm$ remain intact but the S_4 symmetry is broken in the thin film models. We investigate the geometric and electronic structure of these 2D CrO_2 systems, using density functional theory (DFT), within the generalized-gradient approximation,[26−28] as detailed in the Methods section. A series of $(CrO_2)_n/(TiO_2)_m$ superlattice and thin film models with indices $(n-m)$ are considered in our first-principles calculations. Here, the *n* and *m* refer to the number of XO_2 (X = Cr, Ti) formula units per unit cell in the models. With the number of TiO_2 layer (m = 10 for the superlattice and m = 9 for the thin film), an insulator-to-metal transition is observed as the layer number *n* of CrO_2 layer increases, as shown in Figures S1 and S2 of Supporting Information (SI hereafter). During the phase transition, a novel class of half semimetallic Dirac electronic phase emerges in the heterostructures, with n = 4 for the superlattice and n = 5 for the thin film, which will be focused upon in subsequent discussions.

For (4−10) superlattice and (5−9) thin film systems, ferromagnetic (FM) ordering in the 2D CrO_2 layer is energetically favored compared with the antiferromagnetic (AFM) and nonmagnetic ones, similar to the case of bulk CrO_2. The $E_{FM} - E_{AFM} = -214$ and -127 meV/Cr for the superlattice and thin film, respectively. The nonmagnetic configuration is more than 1.2 eV/Cr higher in energy. As shown in Figure 2a,b, these models give rise to clear single-spin

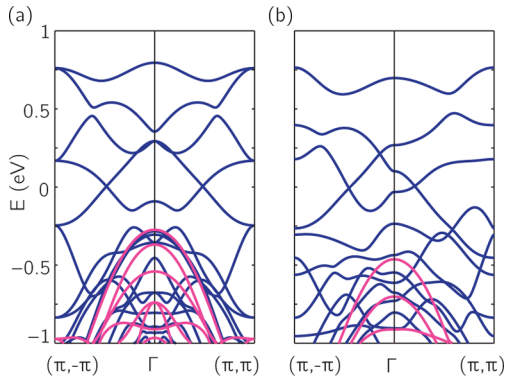

Figure 2. Single-spin Dirac points of CrO_2/TiO_2 interfacial states. (a,b) Nonrelativistic DFT band structure of superlattice and thin film models, respectively. Here, the blue and red bands are for two spins, and the Fermi level is set to zero energy.

Dirac states at the Fermi level, absent other electronic levels in a 0.1−0.2 eV window. Two bands cross the Fermi level at four distinct points, which are along the diagonals of the Brillouin zone (BZ), namely, the path of mirror planes. For the (4−10) superlattice, these crossing points have equal distance away from the center of BZ, located at $\boldsymbol{k}_D = \pm(0.482, \pm 0.482)\pi$. For the (5−9) thin film, four Dirac points are present with unequal distances away from the center of BZ, located at $\pm(0.206, 0.206)\pi$ and $\pm(0.454, -0.454)\pi$. The numerical gaps in the Kohn−Sham bands at the band crossing points $\boldsymbol{k}_D$ are found to be less than 0.1 meV, indicating that the system is truly half-semimetallic, and that the inter-CrO_2 layer coupling between periodic images is vanishingly small. Examining these two bands in the vicinity centered at $\boldsymbol{k}_D$, it is found that away from this point a gap opens linearly. In contrast, Pardo and Pickett[29] proposed that VO_2/TiO_2 nanostructure exhibits half metallic semi-Dirac dispersion, but which does not become completely massless Dirac Fermions.[29] Besides, VO_2 is strongly correlated in the sense that both electron−electron and electron−phonon channels are important,[30] and consequently VO_2 may not be well described by DFT-based calculations within the static lattice approximation. By comparison, DFT in the LDA+U framework is quite successful in describing the basic electronic structure of CrO_2.[31,32] Moveover, these Dirac cones are rather anisotropic, with principal Fermi velocities falling in the range

DOI: 10.1021/acs.nanolett.5b01791
Nano Lett. 2015, 15, 6434−6439

1.0−2.2 × 10^5 m/s, roughly an order of magnitude smaller than that of graphene (see Figure 3a).

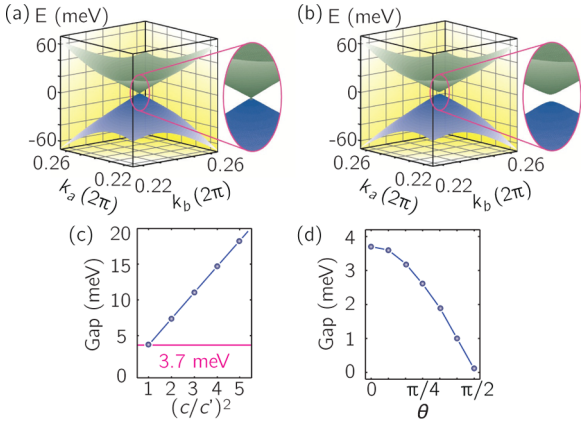

Figure 3. Field-tunable Dirac points in $(CrO_2)_4/(TiO_2)_{10}$ superlattice. (a) The 2D band structure without SOC in the vicinity of a Dirac point. (b) The 2D band structure with SOC in the vicinity of a Dirac point magnetized along *c*-direction. (c) The band gap of the superlattice as a function of the strength of SOC, magnetized along *c*-direction. (d) The band gap of the superlattice with rotating the direction of magnetization from crystallographic [001](θ = 0°) to [110] (θ = 90°) within the (1$\bar{1}$0) plane.

The Dirac points in the above interfacial electronic phase are quite extraordinary, from three points of view. First, they are single-spin Dirac species, unlike graphene that has 2-fold spin degeneracy. Second, these single-spin Dirac points are not located at high-symmetry points, in contrast to typical Dirac systems such as graphene and the surface states of 3-dimensional topological insulators. Third, these Dirac points are field-tunable; that is, they can be massless (gapless) or massive (gapped) depending on straightforward field alignment.

Specifically, the field-tunability of the Dirac points is associated with gap opening by SOC effect, as is introduced in relativistic DFT calculations. When the crystallographic *c*-direction is the spin quantization axis, mirror symmetry ($M_\pm$) is broken. The SOC lifts the degeneracy at the Dirac points, and identical gaps of 3.7 meV are opened up at each Dirac node in the (4−10) superlattice, with S_4 symmetry preserved (see Figure 3a,b). To ascertain that the gap is induced by SOC and is accurately determined, we examine how the gap depends on the strength of SOC. The strength of SOC is characterized by $(c/c')^2$, where c is the speed of light *in vacuo*, and c' the artificially retarded speed of light used in actual calculations. The linearity of gap vs SOC strength plot in Figure 3c gives accurate extrapolation to the band gap at full speed of light, assuring that the gap is induced by SOC and is computed correctly. In the case of (5−9) thin film, SOC opens gaps differently for Dirac points on the diagonal ($k_a = k_b$) and antidiagonal ($k_a = -k_b$) of the BZ. The gap is over 5 meV on the antidiagonal, but about 0.5 meV on the diagonal. The thin film remains semimetallic by the electron−hole compensation between valleys (details in SI).

However, if the superlattice is magnetized by an in-plane field, one expects a momentum shift of the Dirac point rather than gap opening.[33] We have computed the electronic structure of CrO_2/TiO_2 superlattice with in-plane spin quantization along crystallographic [110], [1$\bar{1}$0], [100], and [010] directions (See Table 1 in SI). With a very dense $\boldsymbol{k}$-mesh we find that the gaps in these cases are less than 0.1 meV in all valleys. For the magnetization along [110], gapless Dirac points in the first and third quadrants deviate from the diagonal of the Brillouin zone (BZ), but remain symmetric with respect to M_-. The other two nodes are still on the antidiagonal of BZ but with unequal distances away from the center of BZ. They are expected as M_+ is broken whereas M_- remains intact. For the [1$\bar{1}$0] magnetization, the momentum shift of Dirac points respects the absence of M_- and the presence of M_+. For [100] or [010] magnetization, two broken mirrors lead to lower symmetries of the location of Dirac points. Besides, there is an electron−hole compensation of a few meV between valleys with in-plane magnetization. Figure 3d further shows the band gap of the superlattice gradually increases as the magnetization direction rotates from [110] to *c*-direction, demonstrating that the Dirac states of the interfacial quantum phase can be continuously tuned by rotating the magnetization.

Quantum Anomalous Hall Effect. When $M_\pm$ are broken but S_4 symmetry is preserved, the single-spin massive Dirac states in the superlattice by [001] magnetization will become a nontrivial Chern insulator. It is of interest to quantify the topological character of the SOC-gapped superlattice, by computing the $U(N)$ Berry curvature of Kohn−Sham Bloch states, $\Omega(\boldsymbol{k})$, as[34]

$$\Omega(\mathbf{k})\delta k_a \delta k_b = \mathrm{Arg}\{\det[L_a(\mathbf{k})L_b(\mathbf{k}+\delta\hat{k}_a)L_a^\dagger(\mathbf{k}+\delta\hat{k}_b)L_b^\dagger(\mathbf{k})]\} \quad (1)$$

where $L_\alpha(\boldsymbol{k}) \equiv \vec{u}^\dagger(\boldsymbol{k}) \cdot \vec{u}(\boldsymbol{k}+\delta\hat{\boldsymbol{k}}_\alpha)$ with $\alpha = a,b$ and $\delta\hat{\boldsymbol{k}}_\alpha = \delta k_\alpha \hat{\boldsymbol{e}}_\alpha$. Here, $\vec{u}(\boldsymbol{k}) = [|u_1(\boldsymbol{k})\rangle, ..., |u_N(\boldsymbol{k})\rangle]$, with $u_j(\boldsymbol{k})$ being the cell-periodic part of the Bloch wave function, $\psi_j(\boldsymbol{k})$, of the jth band at $\boldsymbol{k}$. A quadrant of BZ is pixelated into 60 × 60 plaquettes for evaluation of $U(N)$ Berry curvature. A total of 176 bands up to the band gap are considered, below which there is a subvalence gap of about 10 eV. The full zone Berry curvature (see Figure 4a) can be retrieved by imposing S_4 symmetry. Integrating the non-Abelian Berry curvature over the 2-torus BZ yields a Berry

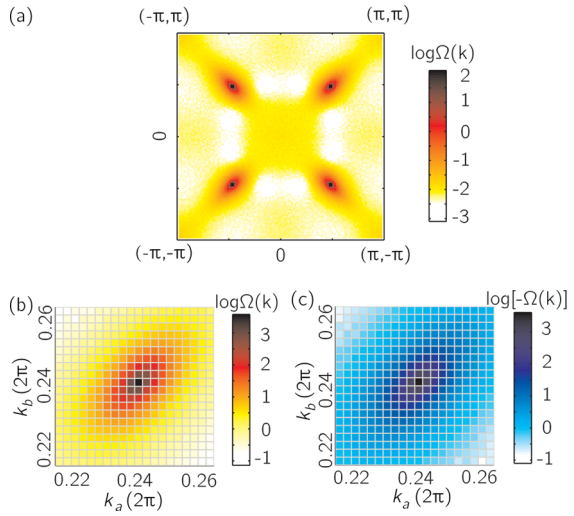

Figure 4. Topological character of Dirac states in the $(CrO_2)_4/(TiO_2)_{10}$ superlattice. (a) The non-Abelian Berry curvature over the entire BZ. The Berry curvature is given in the units of area of real-space unit cell. (b,c) The $U(1)$ Berry curvature of the massive Dirac valley of the highest-occupied valence band and the lowest-unoccupied conduction band, respectively. The $U(1)$ Berry curvatures have opposite signs for the electron and hole excitations.

DOI: 10.1021/acs.nanolett.5b01791
Nano Lett. 2015, 15, 6434−6439

phase of 4.00 π. We note that the Hall conductance, $\sigma_{xy} = (1/2\pi) \int d\mathbf{k}\, \Omega$, where σ_{xy} is given in the units of conductance quantum, e^2/h.[35] Therefore, the interfacial material is a Chern insulator and will exhibit a fully quantized Hall conductance, $\sigma_{xy} = \pm 2.00 e^2/h$. Here, the $\pm$ sign corresponds to the sense of magnetization of the material prior to the Hall measurements.

Figure 4a also shows that the main contribution to the $U(N)$ Berry curvature in the (4−10) superlattice is sharply concentrated around the locations of the four massive Dirac states, indicating that the main source of the anomalous conductivity arises from the SOC gaps. To confirm this, we compute the $U(1)$ Berry curvatures of the valence and conduction bands across the gap, as shown in Figure 4b,c. We see that the massive Dirac Fermion states show prominent $U(1)$ Berry curvature near the gap, with opposite signs for the electron and hole excitations. The integration of the Berry curvature of the highest occupied band in the vicinity of the gap over the small $\boldsymbol{k}$-space region for a single valley encloses a Berry phase of $\sim 0.95 \times \pi$. By the S_4 symmetry of the system, the four valleys will have identical contribution to the Hall conductance. This confirms that the SOC gap dominates the anomalous velocity of Bloch electrons.

Discussion. Given that the spin polarization in CrO_2/TiO_2 heterostructures is inherited from CrO_2, single-spin Dirac states and QAH state may mainly arise from the 2D CrO_2 layer in the heterostructures. To ascertain the origin of novel Dirac electronic phase, we compute the projected electronic density of states/band structure and Kohn−Sham wave functions, which reveal that Dirac states in the heterostructure are indeed contributed by 2D CrO_2 layer (see Figures S3−S6 in SI). While half-metallicity of bulk CrO_2 is already known, these novel quantum states in 2D CrO_2 systems are quite intriguing. Moreover, analyses of the Kohn−Sham wave functions demonstrate that the dominant orbitals of Dirac states are the combination of d_{xz} and d_{yz} orbitals of Cr atoms, of which projection views are shown schematically in Figure 5a, while the other t_{2g} orbital, d_{xy}, is away from the Fermi level. The splitting of t_{2g} orbitals is due to the local D_{2h} symmetry at Cr sites by axial elongation of the octahedron. The same applies to conducting channels close to the Fermi level of bulk CrO_2.[31]

To further confirm the roles of the 2D CrO_2 layer in forming single-spin Dirac states, we now establish the bonding mechanism of the CrO_2 layer (Figure 1a), based on dominant d_{xz} and d_{yz} orbitals of Cr atoms. We consider one single CrO_2 bilayer for simplicity, which contains only two Cr with different heights in a tetragonal unit cell, referred to as sites A and B, respectively. With four Wannier bases, $\{|d_{xz}(A)\rangle, |d_{yz}(A)\rangle, |d_{xz}(B)\rangle, |d_{yz}(B)\rangle\}$, a tight-binding (TB) spinless Hamiltonian, $\mathcal{H}_{\mathbf{k}}$, immediately follows, taking into account the nearest-neighbor (NN) and next nearest-neighbor (NNN) bonding

$$\mathcal{H}_{\mathbf{k}} = \begin{bmatrix} H_{\mathrm{A}} & H_{\mathrm{AB}} \\ H_{\mathrm{AB}}^{\dagger} & H_{\mathrm{B}} \end{bmatrix} \tag{2a}$$

$$H_j = \begin{bmatrix} \varepsilon_j^{xz}(\mathbf{q}) & 0 \\ 0 & \varepsilon_j^{yz}(\mathbf{q}) \end{bmatrix}, \quad j = \mathrm{A},\ \mathrm{B} \tag{2b}$$

$$H_{\mathrm{AB}} = \begin{bmatrix} -2t_3(\cos q_1 + \cos q_2) & 2it_1 \sin q_1 \\ 2it_2 \sin q_2 & 0 \end{bmatrix} \tag{2c}$$

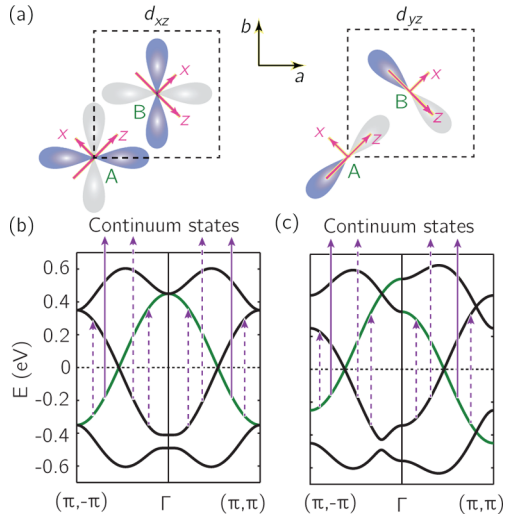

Figure 5. Tight-binding (TB) model of one single CrO_2 bilayer. (a) The Wannier-like basis orbitals considered in our TB model. Left panel: d_{xz} on sites A and B. Right panel: d_{yz} on sites A and B. The lobes of orbitals are colored to show a π phase difference. (b,c) TB band structure of the superlattice and the thin film models, respectively. The green (black) bands correspond to even (odd) mirror eigenstates, with respect to M_+ or M_-. The arrows represent the photoemission or the vertical interband transition. Solid (dashed) arrows stand for light linear polarization parallel (perpendicular) to the corresponding mirror plane.

where $q_{1,2} = (k_a \pm k_b)/2$, and $\varepsilon_j^{\alpha}(\boldsymbol{q}) = E_j^{\alpha} + 4t_j^{\alpha} \cos q_1 \cos q_2$, with $-\pi \le k_a, k_b < \pi$. E_j^{α} are on-site energies and t_j^{α} the NNN hopping, with site index j = A, B and orbital index $\alpha = d_{xz}, d_{yz}$. The NN hopping is described by t_1, t_2, t_3. Notice that t_1 and t_2 do not vanish because sites A and B are not on the same (001) plane. The NN hopping between $|d_{yz}\rangle$'s on sites A and B is zero, as ensured by $M_{\pm}$ mirror planes.

The Hamiltonian proposed above leads to band structures shown in Figure 5b,c, for which the parameters used are given in SI. In Figure 5b, the parameters are chosen respecting the S_4 symmetry, i.e., $E_{\mathrm{A}}^{\alpha} = E_{\mathrm{B}}^{\alpha}$ and $t_{\mathrm{A}}^{\alpha} = t_{\mathrm{B}}^{\alpha}$. We may also break the S_4 symmetry, by setting unequal on-site energies of orbitals of A and B sublattices, as shown in Figure 5c. In both cases, there are four Dirac points arising along the BZ diagonals, with $|k_{Da}| = |k_{Db}|$. The four Dirac points are band contact points between the second and third Bloch bands in energy. They have equal distances away from the center of BZ for the case with S_4 symmetry, while the distances become unequal with a broken S_4 symmetry. These two parameter settings correspond to the superlattice and thin film models, respectively, and indeed give similar band structures with the corresponding first-principles results in Figure 2. Note that the Wannier bases in TB bands with one CrO_2 bilayer considered should be referred to as effective combinations of more d_{xz} and d_{yz} orbitals in CrO_2/TiO_2 heterostuctures, given that the heterostructures include more Cr sites and more effects, such as geometric relaxation. Moreover, when symmetry-allowed NN SOC terms between d_{yz} orbitals on sites A and B are added, the Hamiltonian gives a Chern number of ± 2 and two gapless chiral edge modes within the bulk gap (See SI).

The presence of four degenerate Dirac points away from high-symmetry points in CrO_2/TiO_2 superlattice is very interesting and important to the proposed single-spin Dirac states and QAH state. Then we make a remark upon the role of

DOI: 10.1021/acs.nanolett.5b01791
Nano Lett. 2015, 15, 6434−6439

symmetry of CrO_2/TiO_2 superlattice, which can be generalizable in search of novel Dirac systems. Specifically, it is crucial to realize that the S_4 symmetry is key to the formation of the four Dirac points, akin to the role of inversion symmetry to Dirac points in graphene.[36] We define a unitary matrix associated with the S_4 symmetry, $w_{mn}(\boldsymbol{k}) = \langle u_{m,\hat{S}_4\boldsymbol{k}}|\hat{S}_4|u_{n,\boldsymbol{k}}\rangle$. It can be readily shown that the Berry flux bounded by the first quadrant of BZ is uniquely determined by the w-matrices of $\Gamma(0,0)$ and $M(\pi,\pi)$, as

$$\exp[i\oint_{BZ/4}\mathcal{A}(\mathbf{k})\cdot d\mathbf{k}] = \frac{\det[w(\Gamma)]}{\det[w(M)]} \quad (3)$$

where $\mathcal{A}(\mathbf{k})$ is the Berry connection (see SI). For the spinless Hamiltonian in eq 1, $\det[w(\Gamma)]/\det[w(M)] = -1$ for the lower two bands signifies band inversion with respect to S_4 symmetry between Γ and M, ensuring that a $\pm\pi$ Berry phase is enclosed by a quadrant of BZ. Absent SOC, the $\pm\pi$ Berry phase ensures gaplessness and consequently the formation of Dirac point in each quadrant of BZ, when both S_4 and $M_\pm$ are present. When $M_\pm$ are broken and SOC induces band gaps, the S_4 symmetry ensures that the system is a Chern insulator, with a $\pm4\pi$ Berry phase enclosed by the full BZ. For the thin film model, four Dirac states may survive under the continuous perturbation of the on-site energies. Moreover, $M_\pm$ serves to put the Dirac points along the diagonals of BZ and has interesting consequences. The Bloch states along $\Gamma-(\pi,\pi)$ and $\Gamma-(\pi,-\pi)$, are mirror eigenstates with respect to M_+ and M_-, respectively. The manifestation is optical selectivity in both photoemission and interband transition under linearly polarized light,[37] as shown in Figure 5b,c. It can be well understood by mirror-symmetry analysis on momentum-resolved optical transition matrix element, $\mathcal{P}(\mathbf{k}) = \langle\psi_{f,\mathbf{k}}|\boldsymbol{p}|\psi_{i,\mathbf{k}}\rangle$. Here, $\boldsymbol{p}$ is the momentum operator, along the direction of linearly polarized optical field; ψ_i and ψ_j are the wave functions of initial- and final-state, respectively. When the optical field is parallel (perpendicular) to the mirror plane, $\boldsymbol{p}$ is even (odd) under mirror reflection. For the symmetry-allowed photoemission with a finite matrix element, a even (odd) Bloch initial-state is required with respect to the corresponding mirror plane, given that the final-state is the continuum and seen to be even. Besides, the vertical interband transition can also take place between two Dirac bands with opposite mirror eigenvalues, under the optical field perpendicular to the mirror plane.

Experimentally, the QAH state, arising from single-spin Dirac states, offers a few advantages over the only experimentally established QAH system, which required magnetic doping and showed full quantization of Hall conductance at about 0.03 K.[14] The ferromagnetic CrO_2/TiO_2 does not require additional magnetic impurity atoms, which are a source of scattering and could have lowered the transition temperature. Second, the band gap of the present system corresponds to 43 K, indicating that QAH state may be achieved at considerably higher temperatures. The present system has unique symmetry that ensures its topological character and is composed of two highly industrialized oxides, for which process technologies are rather mature for fabrication of the heterostructure.[24,25]

Conclusion. In summary, we demonstrated that the interfacial electrons at the CrO_2/TiO_2 heterostructures can be fashioned into single-spin Dirac states. In the superlattice model, we can obtain a Chern number = ±2 QAH phase, which will enable dissipationless digital signal transmission with minimal influence of noise. The first-order experiments will include spin-polarized angle-resolved photoemission spectroscopy (ARPES) to characterize these field-tunable Dirac states. Direct Hall measurements on the superlattice samples with out-of-plane magnetization will reveal the conductance plateau,[13,14] which should be robust against weak disorder that may be present in the sample. The optical selectivity in photoemission and interband transition from mirror symmetries can be probed by ARPES[37] and time-resolved ARPES, respectively. Additionally, different substrates, instead of TiO_2, should also be assayed, as stronger SOC of the substrate may further boost the band gap (cf. Figure 3c).

Methods. Our *ab initio* calculations are performed using the projector augmented wave (PAW) method, as implemented in the Vienna *ab initio* Simulation Package (VASP).[27,28] They are based on density-functional theory (DFT) with the generalized gradient approximation (GGA) in the form proposed by Perdew, Burke, and Ernzerhof (PBE).[26] On-site Coulomb interaction is included in the mean-field, rotationally invariant GGA+U approach with U−J = 2 eV for Cr 3d orbitals, as suggested by previous calculations.[31,38] We have also tested different U−J. Within a wide window of U−J, the single-spin Dirac states and quantum anomalous Hall state are robust (see details in SI). A plane-wave cutoff of 520 eV is used. The valence includes 12 electrons for Cr ($3p^63d^54s^1$), 12 for Ti ($3s^23p^63d^24s^2$), and six for O ($2s^22p^4$). The in-plane lattice constant is set to 4.65 Å, i.e., the optimized lattice constant of bulk TiO_2, because TiO_2 layers are constructed as a infinite/semi-infinite substrate to support ultrathin CrO_2 layers in the superlattice/thin film model. Besides, by testing a series of strain, it is seen that the single-spin Dirac states and quantum anomalous Hall state are also robust against strain (see SI). For the ultrathin films, a vacuum layer larger than 16 Å is adopted. We relax the ions toward equilibrium positions until the Hellman−Feynman forces are less than 0.01 eV/Å.

■ ASSOCIATED CONTENT

Supporting Information

The Supporting Information is available free of charge on the ACS Publications website at DOI: 10.1021/acs.nanolett.5b01791.

Additional information on electronic structure of CrO_2/TiO_2 heterostructures, spin−orbit coupling effects on CrO_2/TiO_2 thin film, the in-plane magnetization in CrO_2/TiO_2 superlattice, the parameters used in the tight-binding band structures, the edge states of quantum anomalous Hall effect in CrO_2/TiO_2 superlattice, symmetry and topological origin of Dirac points, evolution of electronic structure with U−J for CrO_2/TiO_2 superlattice, construction of the heterostructures, and evolution of electronic structure with strain (PDF)

■ AUTHOR INFORMATION

Corresponding Authors

*E-mail: jusheng@suda.edu.cn.

*E-mail: jfeng11@pku.edu.cn.

Present Address

#Department of Physics, University of Texas at Austin, Austin, Texas 78712, United States.

Author Contributions

T.C. and X.L. contributed equally to this work.

DOI: 10.1021/acs.nanolett.5b01791
Nano Lett. 2015, 15, 6434−6439

Notes

The authors declare no competing financial interest.

■ ACKNOWLEDGMENTS

The authors are grateful for useful discussions with Profs. Guang-Yu Guo and Junren Shi. This work is supported by the National Science Foundation of China under Grants Nos. 11374220, 11174009, and 11104193, the China 973 Project No. 2013CB921900, 2011CBA00109, and 2014CB920900, the Priority Academic Program Development of Jiangsu Higher Education Institutions, and the Qinlan project of Jiangsu province.

■ REFERENCES

(1) Geim, A. K.; Novoselov, K. S. *Nat. Mater.* **2007**, *6*, 183−191.
(2) Hasan, M. Z.; Kane, C. L. *Rev. Mod. Phys.* **2010**, *82*, 3045−3067.
(3) Volkov, B.; Pankratov, O. *JETP Lett.* **1985**, *42*, 178−181.
(4) Ishibashi, S.; Terakura, K.; Hosono, H. J. *J. Phys. Soc. Jpn.* **2008**, *77*, 053709.
(5) Ran, Y.; Wang, F.; Zhai, H.; Vishwanath, A.; Lee, D.-H. *Phys. Rev. B: Condens. Matter Mater. Phys.* **2009**, *79*, 014505.
(6) Wan, X.; Turner, A. M.; Vishwanath, A.; Savrasov, S. Y. *Phys. Rev. B: Condens. Matter Mater. Phys.* **2011**, *83*, 205101.
(7) Xu, G.; Weng, H.; Wang, Z.; Dai, X.; Fang, Z. *Phys. Rev. Lett.* **2011**, *107*, 186806.
(8) Asano, K.; Hotta, C. *Phys. Rev. B: Condens. Matter Mater. Phys.* **2011**, *83*, 245125.
(9) Burkov, A. A.; Balents, L. *Phys. Rev. Lett.* **2011**, *107*, 127205.
(10) Lu, L.; Fu, L.; Joannopoulos, J. D.; Soljacic, M. *Nat. Photonics* **2013**, *7*, 294−299.
(11) Haldane, F. D. M. *Phys. Rev. Lett.* **1988**, *61*, 2015−2018.
(12) Qi, X.-L.; Wu, Y.-S.; Zhang, S.-C. *Phys. Rev. B: Condens. Matter Mater. Phys.* **2006**, *74*, 085308.
(13) Yu, R.; Zhang, W.; Zhang, H.-J.; Zhang, S.-C.; Dai, X.; Fang, Z. *Science* **2010**, *329*, 61−64.
(14) Chang, C.-Z.; Zhang, J.; Feng, X.; Shen, J.; Zhang, Z.; Guo, M.; Li, K.; Ou, Y.; Wei, P.; Wang, L.-L.; et al. *Science* **2013**, *340*, 167−170.
(15) Xiao, D.; Yao, W.; Niu, Q. *Phys. Rev. Lett.* **2007**, *99*, 236809.
(16) Cao, T.; Wang, G.; Han, W.; Ye, H.; Zhu, C.; Shi, J.; Niu, Q.; Tan, P.; Wang, E.; Liu, B.; et al. *Nat. Commun.* **2012**, *3*, 887.
(17) Xiao, D.; Liu, G.-B.; Feng, W.; Xu, X.; Yao, W. *Phys. Rev. Lett.* **2012**, *108*, 196802.
(18) Li, X.; Cao, T.; Niu, Q.; Shi, J.; Feng, J. *Proc. Natl. Acad. Sci. U. S. A.* **2013**, *110*, 3738−3742.
(19) Chakhalian, J.; Millis, A. J.; Rondinelli, J. *Nat. Mater.* **2012**, *11*, 92−94.
(20) Hwang, H. Y.; Iwasa, Y.; Kawasaki, M.; Keimer, B.; Nagaosa, N.; Tokura, Y. *Nat. Mater.* **2012**, *11*, 103−113.
(21) Xiao, D.; Zhu, W.; Ran, Y.; Nagaosa, N.; Okamoto, S. *Nat. Commun.* **2011**, *2*, 596.
(22) Rüegg, A.; Fiete, G. A. *Phys. Rev. B: Condens. Matter Mater. Phys.* **2011**, *84*, 201103.
(23) Schwarz, K. *J. Phys. F: Met. Phys.* **1986**, *16*, L211−L215.
(24) Kämper, K. P.; Schmitt, W.; Güntherodt, G.; Gambino, R. J.; Ruf, R. *Phys. Rev. Lett.* **1987**, *59*, 2788−2791.
(25) Dedkov, Y.; Fonine, M.; Konig, C.; Rudiger, U.; Guntherodt, G.; Senz, S.; Hesse, D. *Appl. Phys. Lett.* **2002**, *80*, 4181−4183.
(26) Perdew, J. P.; Burke, K.; Ernzerhof, M. *Phys. Rev. Lett.* **1996**, *77*, 3865−3868.
(27) Kresse, G.; Furthmüller, J. *Phys. Rev. B: Condens. Matter Mater. Phys.* **1996**, *54*, 11169−11186.
(28) Kresse, G.; Joubert, D. *Phys. Rev. B: Condens. Matter Mater. Phys.* **1999**, *59*, 1758−1775.
(29) Pardo, V.; Pickett, W. E. *Phys. Rev. Lett.* **2009**, *102*, 166803.
(30) Okazaki, K.; Sugai, S.; Muraoka, Y.; Hiroi, Z. *Phys. Rev. B: Condens. Matter Mater. Phys.* **2006**, *73*, 165116.
(31) Korotin, M. A.; Anisimov, V. I.; Khomskii, D. I.; Sawatzky, G. A. *Phys. Rev. Lett.* **1998**, *80*, 4305−4308.
(32) Korotin, M.; Skorikov, N.; Anisimov, V. *Phys. Met. Metallogr.* **2002**, *94*, 17−23.
(33) Zhang, F.; Kane, C. L.; Mele, E. J. *Phys. Rev. Lett.* **2013**, *110*, 046404.
(34) King-Smith, R. D.; Vanderbilt, D. *Phys. Rev. B: Condens. Matter Mater. Phys.* **1993**, *47*, 1651−1654.
(35) Thouless, D. J.; Kohmoto, M.; Nightingale, M. P.; den Nijs, M. *Phys. Rev. Lett.* **1982**, *49*, 405−408.
(36) Fu, L.; Kane, C. L. *Phys. Rev. B: Condens. Matter Mater. Phys.* **2007**, *76*, 045302.
(37) Zhang, Y.; Chen, F.; He, C.; Zhou, B.; Xie, B. P.; Fang, C.; Tsai, W. F.; Chen, X. H.; Hayashi, H.; Jiang, J.; et al. *Phys. Rev. B: Condens. Matter Mater. Phys.* **2011**, *83*, 054510.
(38) Liechtenstein, A. I.; Anisimov, V. I.; Zaanen, J. *Phys. Rev. B: Condens. Matter Mater. Phys.* **1995**, *52*, R5467−R5470.

DOI: 10.1021/acs.nanolett.5b01791
Nano Lett. 2015, 15, 6434−6439